

1
2
3
4
5
6
7
8
9

DRAFT VERSION JUNE 27, 2018
Typeset using L^AT_EX **manuscript** style in AAS_TE_X62

Suppression of Dielectronic Recombination Due to Finite Density Effects II: Analytical Refinement
and Application to Density Dependent Ionization Balances and AGN Broad Line Emission

10 D. NIKOLIĆ,¹ T. W. GORCZYCA,¹ K. T. KORISTA,¹ M. CHATZIKOS,² G. J. FERLAND,² F. GUZMÁN,²
11 P. A. M. VAN HOOF,³ R. J. R. WILLIAMS,⁴ AND N. R. BADNELL⁵

12 ¹*Western Michigan University, Kalamazoo, MI, USA*

13 ²*University of Kentucky, Lexington, KY, USA*

14 ³*Royal Observatory of Belgium, Ringlaan 3, 1180 Brussels, Belgium*

15 ⁴*AWE plc, Aldermaston, Reading RG7 4PR, UK*

Corresponding author: T. W. Gorczyca
thomas.gorczyca@wmich.edu

dragan.nikolic@wmich.edu

thomas.gorczyca@wmich.edu

kirk.korista@wmich.edu

mchatzikos@gmail.com

gary@uky.edu

francisco.guzman@uky.edu

p.vanhoof@oma.be

⁵*University of Strathclyde, Glasgow, UK*

(Received; Revised)-; Accepted;)-

ABSTRACT

We present improved fits to our treatment of suppression of dielectronic recombination at intermediate densities. At low densities, most recombined excited states eventually decay to the ground state, and therefore the total dielectronic recombination rate to all levels is preserved. At intermediate densities, on the other hand, collisions can lead to ionization of higher-lying excited states, thereby suppressing the dielectronic recombination rate. The improved suppression factors presented here, although highly approximate, allows summed recombination rate coefficients to be used to intermediate densities. There have been several technical improvements to our previously presented fits. For H- through B-like ions the activation log densities have been adjusted to better reproduce existing data. For B-, C-, Al-, Si-like ions secondary autoionization is now included. The treatment of density discontinuity in electron excitations out of ground state H-, He-, and Ne-like ions has been improved. These refined dielectronic recombination suppression factors are used in the most recent version of plasma simulation code Cloudy. We show how the ionization and emission spectrum changes when this physics is included. Although these suppression factors improve the treatment of intermediate densities, they are highly approximate and are not a substitution for a complete collisional radiative model of the ionization balance.

Keywords: atomic data, atomic processes, line: formation, plasmas, ISM: atoms, ISM: abundances, galaxies: nuclei

1. INTRODUCTION

DR is an important process determining the ionization balance in cosmic plasmas. To this end, a large effort has been devoted to computing a reliable database for total and partial DR rate coefficients

41 (see [Badnell et al. 2003](#), and the 14 subsequent papers in that series, as referenced by the latest one,
42 [Kaur et al. \(2017\)](#)). These data are necessary input to plasma simulation codes such as Cloudy
43 ([Ferland et al. 2017](#)). However, all of that data has been computed assuming a zero-density plasma
44 environment, reducing the total DR problem to a more tractable atomic physics problem consisting
45 of a single incoming electron colliding with a single atomic ion and recombining to an ionization state
46 one lower in charge, with the emission of one photon (and any additional, cascading photons).

47 It has long been recognized ([Burgess & Summers 1969](#)) that in a plasma of non-negligible density,
48 such as in the broad emission-line regions of Active Galactic Nuclei, with densities $n_e \sim 10^{10} \text{ cm}^{-3}$,
49 additional, secondary plasma electrons enter into the problem and may affect the total recombination
50 rate via intermediate electron-impact ionization of captured, doubly-excited resonance states, deplet-
51 ing the radiative rate and thereby the final recombination probability. Treating this more complex
52 problem requires, in addition to accurate, zero-density atomic data, a generalized collisional radia-
53 tive (GCR) model approach ([Summers & Hooper 1983](#)) to account for all possible recombination and
54 ionization pathways.

55 To date, there has been limited GCR modeling carried out, and we have relied on the pioneer-
56 ing work of [Burgess & Summers \(1969\)](#), and the extensive, detailed calculations for the density-,
57 temperature-, and elemental-dependent, effective recombination rate coefficient of [Summers \(1974](#)
58 [& 1979\)](#), as a guide for quantifying the suppression of DR due to finite-density effects. This was
59 the approach adopted by us in a previous publication [Nikolić et al. \(2013\)](#), hereafter referred to as
60 Paper I.

61 After several model applications of this algorithm, it was found in certain situations (see for example
62 [Young \(2018\)](#)), that the original formulation was susceptible on finer grids to numerical difficulties
63 arising from a discontinuity in temperature of the effective DR rate coefficient. This problem affects
64 the first five isoelectronic sequences: H- through B-like.

65 The present paper serves three purposes. First, a minor “tweak” to our previous formulation is
66 introduced to circumvent the earlier discontinuity in temperature of the suppression factor. Second,
67 to provide an alternative suppression factor for four sequences, following [Summers \(1974 & 1979\)](#),

68 depending on the source of (physics included in) the zero-density DR rate coefficients it is to be
 69 applied to. Third, representative finite-density plasma simulations are carried out using the new,
 70 modified Cloudy version to assess the effect of finite densities, via the consequent DR suppression,
 71 in an actual plasma environment.

72 2. GENERALIZED DENSITY SUPPRESSION MODEL

73 The present approach for treating DR suppression follows closely the original formulation of [Nikolić](#)
 74 [et al. \(2013\)](#), with only minor refinement in the final algorithm, but for completeness and to avoid any
 75 confusion, the entire formulation is repeated below, with the important modification highlighted. In
 76 general, the *effective* DR rate coefficient $\alpha_{\text{DR}}^{\text{eff}}(n_e, T, q, N)$, as a function of electron density n_e (cm^{-3})
 77 and temperature T (K), ionic charge state q , and isoelectronic sequence (labeled by N) is suppressed
 78 from the zero-density value $\alpha_{\text{DR}}(T)$ (cm^3s^{-1}) by a dimensionless suppression factor $S^N(n_e, T; q)$,

$$\alpha_{\text{DR}}^{\text{eff}}(n_e, T, q, N) \equiv S^N(n_e, T; q) \alpha_{\text{DR}}(T) \quad ; \quad (1)$$

79 for simplicity, we use the dimensionless log density parameter $x = \log_{10} n_e$.

The functional form of $S^N(n_e, T, q)$ is taken to be a pseudo-Voigt profile

$$S^N(x, T; q) = \begin{cases} 1 & x \leq x_a(T; q, N) \\ e^{-\left(\frac{x-x_a(T; q, N)}{w/\sqrt{\ln 2}}\right)^2} & x \geq x_a(T; q, N) \end{cases}, \quad (2)$$

80 of width $w = 5.64586$ and an activation log density $x_a(T; q, N)$ that is represented by the complicated
 81 expression

$$x_a(T; q, N) = x_a^0 + \log_{10} \left[\left(\frac{q}{q_0(q, N)} \right)^7 \left(\frac{T}{T_0(q, N)} \right)^{1/2} \right]. \quad (3)$$

82 A fit of the suppression factors of [Summers \(1974 & 1979\)](#) for all ions yielded a global (log) activation
 83 density $x_a^0 = 10.1821$ and more complicated expressions for the zero-point temperature T_0 (K) and
 84 charge state q_0 . These were found to depend on both the ionic charge state q and the isoelectronic
 85 sequence N viz.

$$T_0(q, N) = 5 \times 10^4 [q_0(q, N)]^2 \quad (4)$$

86 and

$$q_0(q, N) = (1 - \sqrt{2/3q})A(N)/\sqrt{q}, \quad (5)$$

87 where

$$A(N) = 12 + 10N_1 + \frac{10N_1 - 2N_2}{N_1 - N_2}(N - N_1) \quad (6)$$

88 depends on the isoelectronic sequence in the periodic table according to the specification of the
89 parameters

$$(N_1, N_2) = \begin{pmatrix} (3, 10) N \in 2^{nd} \text{ row} & (37, 54) N \in 5^{th} \text{ row} \\ (11, 18) N \in 3^{rd} \text{ row} & (55, 86) N \in 6^{th} \text{ row} \\ (19, 36) N \in 4^{th} \text{ row} & (87, 118) N \in 7^{th} \text{ row} \end{pmatrix}. \quad (7)$$

90 If the zero-density DR data $\alpha_{\text{DR}}(T)$ in Eq. (1) neglects the secondary autoionization (Blaha 1972), this
91 parametrization is sufficient for all isoelectronic sequences $N \geq 6$. However, the given parametrization
92 was not flexible enough to provide an adequate fit to the Summers (1974 & 1979) data for the lower
93 isoelectronic sequences $N \leq 5$. Instead, we explicitly list the optimal values for $A(N)$, for lower
94 ionization stages, in Table 1.

95 Even with this formulation, an additional modification was necessary at electron temperatures
96 and/or ionic charges for which the q -scaled temperature $\theta \equiv T/q^2$ was very low ($\theta \leq 2.5 \times 10^4$ K,
97 which is now a slightly different formulation than that used previously.

98 In Paper I Nikolić et al. (2013), we modified the factor $A(N)$ for low temperatures as follows:

$$A^{mod,old}(N \leq 5) = \begin{cases} A(N), & \theta > 2.5 \times 10^4 \text{ K} \\ 2 \times A(N), & \theta \leq 2.5 \times 10^4 \text{ K} \end{cases}. \quad (8)$$

99 Using this algorithm, the discontinuity in the modification factor, from unity to a factor of two at
100 $\theta = T/q^2 = 2.5 \times 10^4$ K, was found to cause numerical difficulties, for certain density-dependent
101 modeling applications, using the previous Cloudy release following Paper I. In order to avoid any
102 such algorithmic difficulties in the future, and also to allow for an improved fit of the available

103 suppression factor data of [Summers \(1974 & 1979\)](#) by a generalized suppression formulation, we
 104 update the additional low-temperature modification factor via a continuous function:

$$A^{mod}(N) = \begin{cases} \psi^N(q, T) \times A(N), & N \leq 5 \\ \psi_{sec}^N(q, T) \times A(N), & N = 5, 6, 13, 14 \end{cases}. \quad (9)$$

105 Here the additional dimensionless functions

$$\psi^N(q, T) = 2 \times \frac{1 + \pi_3 \times e^{-\left(\frac{\log_{10} T - \pi_1}{\sqrt{2}\pi_2}\right)^2} + \pi_6 \times e^{-\left(\frac{\log_{10} T - \pi_4}{\sqrt{2}\pi_5}\right)^2}}{1 + e^{-\sqrt{25000q^2/T}}} \quad (10)$$

$$\pi_i = \pi_i^{(1)} + \pi_i^{(2)} \times q^{\pi_i^{(3)}} \times e^{-q/\pi_i^{(4)}} \quad i = 1 \dots 6,$$

106

$$\psi_{sec}^N(q, T) = 1 + \gamma_3 \times e^{-\left(\frac{\log_{10} T - \gamma_1}{\sqrt{2}\gamma_2}\right)^2} + \gamma_6 \times e^{-\left(\frac{\log_{10} T - \gamma_4}{\sqrt{2}\gamma_5}\right)^2} \quad (11)$$

$$\gamma_i = \gamma_i^{(1)} + \gamma_i^{(2)} \times q^{\gamma_i^{(3)}} \times e^{-q/\gamma_i^{(4)}} \quad i = 1 \dots 6,$$

107 are continuous at all temperatures and ensure the same asymptotic behavior as determined before,

$$A^{mod}(N) \xrightarrow{\theta \rightarrow \infty} A(N) \quad (12)$$

$$\xrightarrow{\theta \rightarrow 0} 2 \times A(N), \quad (13)$$

108 and the additional flexibility introduced allows for an improved fit to the [Summers \(1974 & 1979\)](#)
 109 data; the adjustment coefficients $\pi_i^{(j)}$ and $\gamma_i^{(j)}$ are given in [Table 2](#) and the $\psi^N(q, T)$ for iso-electronic
 110 sequences considered here are illustrated in [Fig. 4](#) of [Appendix A](#).

111 If the main concern is to remove the temperature discontinuity, while keeping the overall agreement
 112 with [Summers \(1974 & 1979\)](#) data to better than 25%, then we suggest using the “simplified” part
 113 of [Table 2](#). However, for the overall agreement with [Summers \(1974 & 1979\)](#) data of 14% and better,
 114 the use of “detailed” part of [Table 2](#) is recommended for lowest five isoelectronic sequences. For the
 115 B-, C-, Al-, and Si-like sequences effects of secondary autoionization cannot be neglected. If the zero-
 116 density DR data $\alpha_{DR}(T)$ in [Eq. \(1\)](#) for these isoelectronic sequences already accounts for secondary
 117 autoionization effects, then the “secondary autoionization” part of [Table 2](#) should be used. Note

Table 1. Modified $A(N)$ coefficients from Eq. (6).

Sequence	N	$A(N)^\dagger$	Sequence	N	$A(N)^\ddagger$
No secondary autoionization			Secondary autoionization included		
H-like	1	16	B-like	5	52
He-like	2	18	C-like	6	37.7
Li-like	3	66	Al-like	13	100.9
Be-like	4	66	Si-like	14	90.3
B-like	5	52			

[†] these must be multiplied by $\psi^N(q, T)$ given in Eq. (10)

[‡] these must be multiplied by $\psi_{sec}^N(q, T)$ given in Eq. (11)

118 that Table 2 contains two sets of adjustment coefficients for B-like ions, depending on whether the
 119 zero-density DR data $\alpha_{DR}(T)$ in Eq. (1) already contains corrections due to secondary autoionization
 120 or not. The results of Paper I should be used for all other isoelectronic sequences, including C-,
 121 Al- and Si-like if being applied to zero-density DR rate coefficients which do not include secondary
 122 autoionization. In the 2017 release of Cloudy (Ferland et al. 2017) the zero-density DR data for B-
 123 like ions is modified using the “secondary autoionization” part of Table 2 in accordance with modern
 124 DR data of Badnell et al. (2003)¹ which includes the effect. For details regarding the variation of
 125 accuracy with respect to approximations used over a wide range of temperatures and isoelectronic
 126 sequences see Fig. 5 of Appendix B.

127 To illustrate how much better the present algorithm reproduces the Summers (1974 & 1979) sup-
 128 pression factor, we show a comparison of old and new results in Fig. 1 for several representative ions,
 129 sequences, and temperatures as a function of electron density.

130 For even lower temperatures, we add a final modification to ensure that, at plasma energies kT
 131 much less than the excitation energies, $\epsilon_N(q)$, for which the intermediate resonance states are not

¹ H- through Si-like data is available from <http://amdpp.phys.strath.ac.uk/tamoc/DATA/DR/>

Table 2. Adjustment coefficients $\pi_i^{(j)}$ from Eq. (10) and $\gamma_i^{(j)}$ from Eq. (11).

adjustment factor:		“detailed” $\psi^N(q, T)$				“simplified” ψ				“secondary autoionization” $\psi_{\text{sec}}^N(q, T)$							
Sequence	N	π_i	$\pi_i^{(1)}$	$\pi_i^{(2)}$	$\pi_i^{(3)}$	$\pi_i^{(4)}$	$\pi_i^{(1)}$	$\pi_i^{(2)}$	$\pi_i^{(3)}$	$\pi_i^{(4)}$	Sequence	N	γ_i	$\gamma_i^{(1)}$	$\gamma_i^{(2)}$	$\gamma_i^{(3)}$	$\gamma_i^{(4)}$
H-like	1	π_1	4.7902	0.32456	0.97838	24.78084	0	0	0	∞	C-like	6	γ_1	5.90184	-1.2997	1.32018	2.10442
		π_2	-0.0327	0.13265	0.29226	∞	∞	0	0	∞			γ_2	0.12606	0.009	8.33887	0.44742
		π_3	-0.66855	0.28711	0.29083	6.65275	0	0	0	∞			γ_3	-0.28222	0.018	2.50307	3.83303
		π_4	6.23776	0.11389	1.24036	25.79559	0	0	0	∞			γ_4	6.96615	-0.41775	2.75045	1.32394
		π_5	0.33302	0.00654	5.67945	0.92602	∞	0	0	∞			γ_5	0.55843	0.45	0.0	2.06664
		π_6	-0.75788	1.75669	-0.63105	184.82361	0	0	0	∞			γ_6	-0.17208	-0.17353	0.0	2.57406
He-like	2	π_1	4.82857	0.3	1.04558	19.6508	0	0	0	∞	Al-like	13	γ_1	6.59628	-3.03115	0.0	10.519821
		π_2	-0.50889	0.6	0.17187	47.19496	∞	0	0	∞			γ_2	1.20824	-0.85509	0.21258	25.56
		π_3	-1.03044	0.35	0.3586	39.4083	0	0	0	∞			γ_3	-0.34292	-0.06013	4.09344	0.90604
		π_4	6.14046	0.15	1.46561	10.17565	0	0	0	∞			γ_4	7.92025	-3.38912	0.0	10.02741
		π_5	0.08316	0.08	1.37478	8.54111	∞	0	0	∞			γ_5	0.06976	0.6453	0.24827	20.94907
		π_6	-0.19804	0.4	0.74012	2.54024	0	0	0	∞			γ_6	-0.34108	-0.17353	0.0	6.0384
Li-like	3	π_1	4.55441	0.08	1.11864	∞	0	0	0	∞	Si-like	14	γ_1	5.54172	-1.54639	0.01056	3.24604
		π_2	0.3	2.0	-2.0	67.36368	∞	0	0	∞			γ_2	0.39649	0.8	3.19571	0.642068
		π_3	-0.4	0.38	1.62248	2.78841	0	0	0	∞			γ_3	-0.35475	-0.08912	3.55401	0.73491
		π_4	4.00192	0.58	0.93519	21.28094	0	0	0	∞			γ_4	6.88765	-1.93088	0.23469	3.23495
		π_5	0.00198	0.32	0.84436	9.73494	∞	0	0	∞			γ_5	0.58577	-0.31007	3.30137	0.83096
		π_6	0.55031	-0.32251	0.75493	19.89169	0	0	0	∞			γ_6	-0.14762	-0.16941	0.0	18.53007
Be-like	4	π_1	2.79861	1.0	0.82983	18.05422	0	0	0	∞							
		π_2	-0.01897	0.05	1.34569	10.82096	∞	0	0	∞							
		π_3	-0.56934	0.68	0.78839	2.77582	0	0	0	∞							
		π_4	4.07101	1.0	0.7175	25.89966	0	0	0	∞							
		π_5	0.44352	0.05	3.54877	0.94416	∞	0	0	∞							
		π_6	-0.57838	0.68	0.08484	6.70076	0	0	0	∞							
B-like	5	π_1	6.75706	-3.77435	0.0	4.59785	0	0	0	∞	B-like	5	γ_1	6.91078	-1.6385	2.18197	1.45091
		π_2	0.0	0.08	1.34923	7.36394	∞	0	0	∞			γ_2	0.4959	-0.08348	1.24745	8.55397
		π_3	-0.63	0.06	2.65736	2.11946	0	0	0	∞			γ_3	-0.27525	0.132	1.15443	3.79949
		π_4	7.74115	-4.82142	0.0	4.04344	0	0	0	∞			γ_4	7.45975	-2.6722	1.7423	1.19649
		π_5	0.26595	0.09	1.29301	6.81342	∞	0	0	∞			γ_5	0.51285	-0.60987	5.15431	0.49095
		π_6	-0.39209	0.07	2.27233	1.9958	0	0	0	∞			γ_6	-0.24818	0.125	0.59971	8.34052

132 suppressed (see Paper I), the suppression is “turned off”:

$$S^N(x, T; q) = 1 - [1 - S^N(x, T; q)] \times \exp\left(-\frac{\epsilon_N(q)}{10kT}\right). \quad (14)$$

133 When compared to the Paper I methodology for H-, He-, and Ne-like ions, in the present study we
 134 “turn off” the suppression for these ions in continuous fashion with respect to the global activation log
 135 density x_a^0 , see Table 5 of Appendix C. We also update the excitation energy $\epsilon_{14}(2)$ for S^{2+} following
 136 the results of [Badnell et al. \(2015\)](#). The excitation energies for other isoelectronic sequences remain

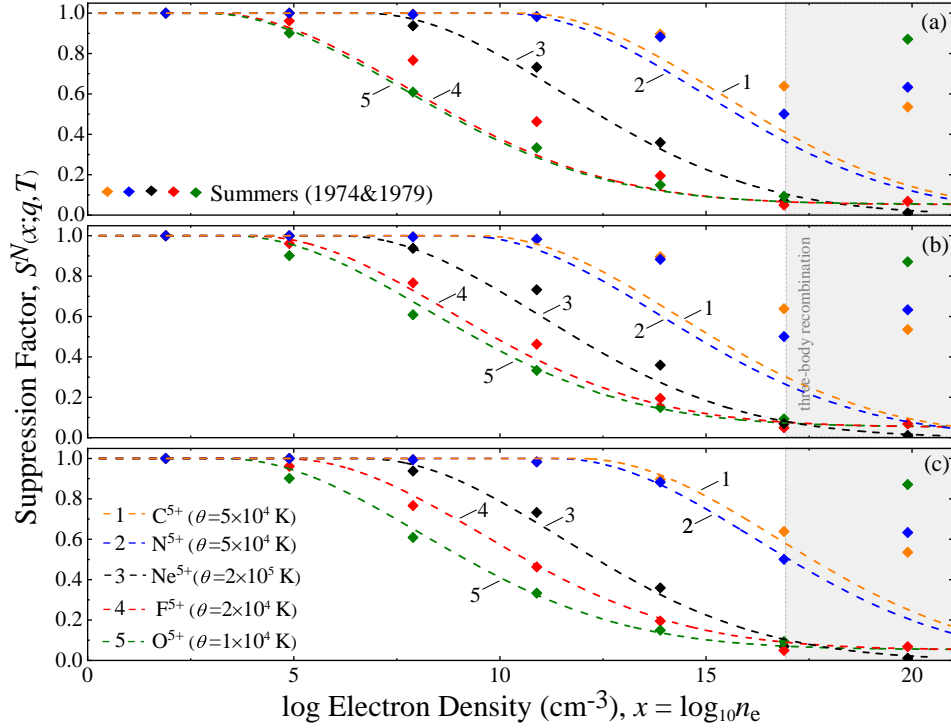


Figure 1. Computed suppression factors for representative situations (ions, sequences, temperatures, and densities) as compared to the GCR results of Summers (1974 & 1979). Results correspond to cases when activation log density $x_a(T; q, N)$ is estimated using the earlier formulation of Paper I (a), the “simplified” ψ (b), or the “detailed” $\psi^N(q, T)$ (c) adjustment factors given in Eq. (10) and Table 2.

137 the same as in Paper I, parameterized by the expression

$$\epsilon_N(q) = \sum_{j=0}^5 p_{N,j} \left(\frac{q}{10} \right)^j . \quad (15)$$

138 As in Paper I, these parameters are optimized using the available NIST excitation energies (Ralchenko
139 et al. 2011) and are listed in Table 5 of Appendix C.

140 3. IONIZATION AND EMISSION PREDICTIONS

141 The density dependence of the ionization rate coefficient at most astrophysical densities is negligible
142 compared to that of the (dielectronic) recombination one - see e.g. Sec. 3.2, p.5 of Summers (1974 &
143 1979). This is a reasonable approximation since the initial state population for ionization is almost
144 exclusively in the ground (and perhaps metastables), which have little density dependence, compared
145 to excited states. In contrast, density dependence in recombination arises via the final state, and in

146 DR these are highly-excited. The effective "density dependent" ionization rate coefficients can be
147 downloaded from Open ADAS (Summers 2004) in ADF11 data format at two degrees of refinement:
148 (i) 'unresolved', in which ions are assumed to be in the ground state only, and (ii) 'metastable-
149 resolved', in which both ground and metastable states of ions may be dominant. Section D of
150 Appendix presents the ionization balance for the lightest thirty elements for the photoionization and
151 collisional ionization cases.

152 3.1. *The equivalent two-level approximation*

153 Several approaches can be taken in computing the ionization distribution of the elements. In the
154 equivalent two-level approximation, which applies at low densities, recombinations to excited states
155 will eventually decay to the ground state. Only ionizations from ground need to be considered since
156 at low densities this is where nearly all of the population lies. This approximation holds for the
157 interstellar medium (ISM) and is described in texts such as (Osterbrock & Ferland 2006, hereafter
158 AGN3), and in Section 3.2 of (Ferland et al. 2017, hereafter C17). In this approximation summed
159 recombination coefficients, such as those given at <http://amdpp.phys.strath.ac.uk/tamoc/DATA>,
160 can be used. At high densities, the gas comes into LTE and the ionization is given by the Saha-
161 Boltzmann equation. This limit is reached in the lower parts of many stellar atmospheres and
162 accretion disks (Hubeny & Mihalas 2014). The intermediate density case is the most difficult since
163 neither limit applies and collisional processes affecting the highly-excited Rydberg levels must be
164 taken into account. In this case a "collisional radiative model" (CRM) must be done. Such models
165 are discussed in Ralchenko (2016) and Section 3.1 of C17. Section 3 of C17 used Cloudy's full CRM
166 treatment of one and two electron systems to make estimates of the range over which the two-level
167 and LTE approximations hold. The ranges are significantly different for collisionally and photoionized
168 environments. CRM effects are important at much lower densities in the collisional case due to the
169 dominance of near-threshold collisional ionization, which also affect the Rydberg level populations.
170 In the photoionized case, the gas kinetic temperature is much lower than the ionization potentials
171 so collisional ionization is much less important. The range over which the two-level approximation

172 works is also very strongly density dependent. The two-level approximation works at much higher
 173 densities for higher charges q due to the well-know q^{-7} scaling of collisional effects, described by
 174 [Bates et al. \(1962\)](#) and [Burgess & Summers \(1969\)](#). This paper develops corrections to the summed
 175 recombination coefficients to improve the behavior of the two-level approximation at intermediate
 176 densities. The results of this paper are included in the C17.01 update to Cloudy and we use that
 177 version in the calculations presented here.

178 3.2. *The case of Oxygen*

179 We first focus on oxygen since it is the third most common element, has high quality DR rates,
 180 and produces strong emission lines from the IR to the X-ray so has great astronomical importance.
 181 Figure 2 shows the suppression factors for the first seven ionization stages of oxygen. These were
 182 computed for a gas kinetic temperature of $10^{4.5}$ K and various electron densities, indicated along the
 183 independent-axis. This low temperature is characteristic of photoionized plasmas with a moderate
 184 level of ionization and is chosen to illustrate the physics.

186 The density and charge dependencies reflect the decays of the highly excited levels. Suppression is
 187 negligible for densities below $\sim 10^4$ cm $^{-3}$. For very low densities, the collisional rate is much slower
 188 than the radiative decay rates so electrons captured into Rydberg levels will undergo a stabilizing
 189 radiative decay and the ion recombines. The detailed density dependence is different for different
 190 ions because the electron configuration affects the detailed stabilization channels, but the tendency
 191 is for the importance of suppression to decrease with increasing ionization, a tendency also shown for
 192 the one and two electron species in Section 3 of C17. The radiative decay rates, which stabilize the
 193 recombined ion, have a rapid charge dependence, $\sim q^4$, while the collisional ionization rate coefficients
 194 decrease. So, for higher charge q higher densities are needed to obtain the same suppression effect,
 195 according to the $\sim q^{-7}$ effect discussed by [Bates et al. \(1962\)](#) and [Burgess & Summers \(1969\)](#).
 196 The remainder of this section develops collisional- and photoionized models with and without this
 197 suppression to study its effects on spectroscopic models. We note that [Summers \(1974 & 1979\)](#) did
 198 not provide any finite-density data for the recombination of singly-charged ions to form neutrals.

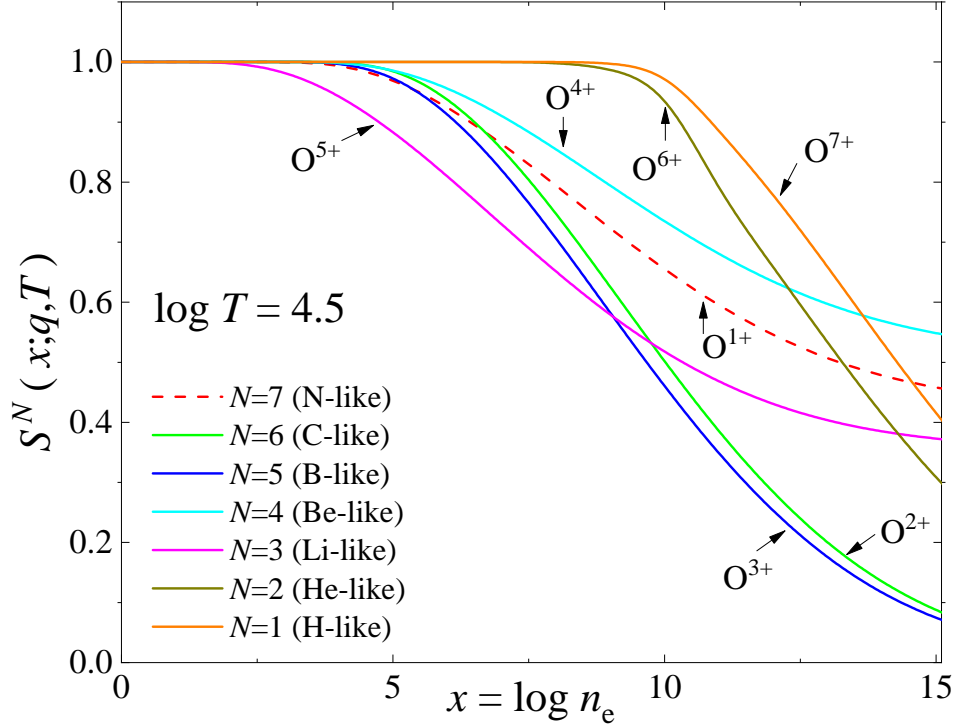


Figure 2. Suppression of oxygen DR for various ions and a temperature of $10^{4.5}$ K. The legend indicates the isoelectronic sequence of the recombining species, with O^{1+} indicating recombination forming O I or O^0 . The logarithm of electron density is indicated along the independent-axis.

199 Consequently, results for neutrals should be treated with extreme caution since they follow from
 200 extrapolation of doubly- to singly-charged data.

201 3.3. Ionization calculations for the lightest thirty elements

202 We consider two classes of models: the first are in electron collisional ionization equilibrium, while
 203 the second is for a photoionized gas. We note that a significant amount of C, O, Si, and S form
 204 molecules in the lowest temperature and electron density collisional model. Although physically
 205 correct, this introduces a distraction from our main point, the density-dependent effect of DR sup-
 206 pression upon the ionization. The chemistry network was disabled for the calculations presented
 207 here, which has the added benefit of decoupling the results from uncertainties in the chemical rates
 208 and the completeness of the chemical database. We concentrate now on oxygen and show results in
 209 Figure 3.

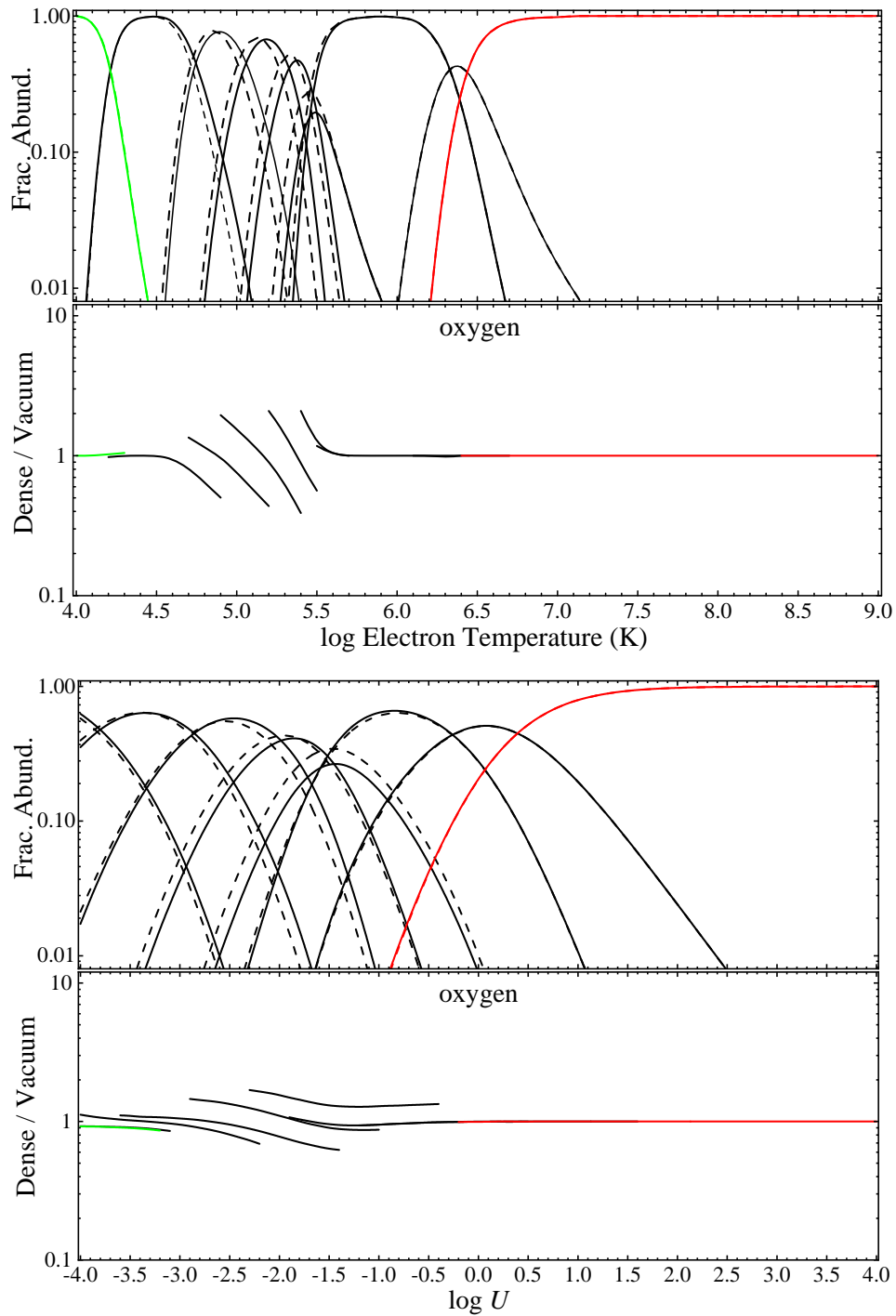


Figure 3. Ionization results for oxygen for the two cases. Section D of Appendix shows similar results for the lightest thirty elements. The upper pair of panels is for a collisionally ionized gas and the independent axis is the gas temperature. The lower pair of panels is for photoionization and the ionization parameter is the independent axis. In each, the upper sub-panel shows the ionization at densities of 1 cm^{-3} (vacuum, solid line) and 10^{10} cm^{-3} (dense, dashed line) while the lower sub-panel shows their ratio.

211 In the electron collisional case, ionizing photons can be neglected and only impact ionization by
 212 thermal electrons is important. Ionization by other particles such as protons and helium nuclei are
 213 included but are generally negligible. As shown in the discussion around equation Eq. 4 of C17, the
 214 ionization fraction has no direct density dependence if the collisional ionization and recombination
 215 rate coefficients do not depend on density. The ionization fraction depends only on the temperature
 216 due to the exponential dependence of the Boltzmann factor in the collisional ionization rate coefficient
 217 and the slower temperature dependencies of the recombination rate coefficients. Higher ionization
 218 is produced by higher temperatures, the free parameter in this case. The temperature is varied
 219 over a very wide range so that the charge state of most elements ranges from fully atomic at low
 220 temperatures to bare nuclei at high values.

We also consider photoionized clouds. Here the radiation field is the dominant source of ioniza-
 tion. The photoionization rate has no temperature dependence so the recombination rate coefficients
 introduce the only direct temperature dependence. That temperature is determined by the balance
 between heating and cooling processes, as discussed in Chapter 3 of AGN3. Increases in the ioniza-
 tion are produced by either a brighter radiation field, which increases the photoionization rate, or by
 a smaller electron density, which decreases the recombination rate. The ionization parameter U , the
 dimensionless ratio of photon to hydrogen densities, (AGN3, Eq. 14.7), is defined as

$$U \equiv \frac{Q(\text{H})}{4\pi r^2 n(\text{H}) c} \equiv \frac{\Phi(\text{H})}{n(\text{H}) c}, \quad (16)$$

221 where $Q(\text{H})$ is the total number of ionizing photons, r the separation between the radiation source
 222 and the cloud, and $\Phi(\text{H})$ is the flux of hydrogen-ionizing photons, $n(\text{H})$ is the number density of
 223 hydrogen, and c is the speed of light. This parameter plays the same role as the temperature in the
 224 collisional case. We vary U over a broad range to change the ionization from atomic to fully ionized.
 225 The gas is irradiated by a continuum with $f_\nu \propto \nu^{-1}$ between 30 meV and 100 MeV.

226 In photoionization equilibrium, the gas temperature depends on the ionization parameter in a
 227 complex way but generally tends to increase with U and, at constant U , increase with density due to
 228 suppression of collisional cooling at high densities. These temperature changes would obfuscate the

229 central point of this paper, the density-dependent suppression, since we wish to compare models with
 230 different densities which will have different temperatures. To remove this confusion, we artificially
 231 set the gas kinetic temperature to an intermediate value, $T = 10^{4.5}$ K, for all U and both densities.
 232 A density of $n_e = 1 \text{ cm}^{-3}$ is used to represent the vacuum case. As shown in Figure 2, DR is not
 233 suppressed at such low densities. A density of $n_e = 10^{10} \text{ cm}^{-3}$ represents an interesting intermediate
 234 density. Figure 2 shows that the DR is moderately suppressed at this density. The density is typical
 235 of the broad emission-line regions of Active Galactic Nuclei (Korista et al. 1997) and is a low-to-
 236 intermediate density in terms of the CRM. This density is low enough that the CRM effects are
 237 significant but not dominant, so a modified two-level approximation should apply.

238 Suppression of the recombination coefficients will cause the ionization to increase in the two-level
 239 limit. A corrected two-level approximation might then reproduce the intermediate-density rise in the
 240 ionization shown in Figs 10 & 11 of C17. For these densities, the CRM effects are not yet large and the
 241 two-level approximation, with modified recombination coefficients, is a reasonable approximation. At
 242 very high densities, where CRM effects are severe, the gas ionization goes over to the Saha-Boltzmann
 243 limit and decreases as density increases. It would be unrealistic to hope that simple corrections to
 244 the two-level approximation could recover this limit.

245 Figure 3 and Figures A and B of Appendix D show results. The upper panel shows ionization
 246 fractions, the dimensionless ratio $n(\text{ion})/n(\text{element})$. The series of peaks corresponds to successively
 247 higher stages of ionization reaching an abundance peak at a particular temperature or ionization
 248 parameter. In the electron collisional case, the temperature of this peak is determined mainly by the
 249 ionization potential, the details of the collisional ionization and recombination rate coefficients, and
 250 the density suppression of the latter. In the photoionization case, the peak is sensitive to both the
 251 ionization parameter and the shape of the incident radiation field, in addition to the photoionization
 252 cross section and recombination rate coefficients. The lower panel shows the ratio of the ionization
 253 fractions for the two densities to make the changes in the ionization easier to see. Predictions change
 254 by approximately a factor of two for O, although other elements can have an order of magnitude
 255 change, as Figures A and B of Appendix D show. The changes are largest for intermediate ion-

256 ization stages of O, reflecting the suppression factors shown in Figure 2. The general trend for the
 257 other elements is for the changes to be largest for lower ionization stages and tend to decrease with
 258 increasing charge, as suggested by the q^{-7} dependence discussed in Burgess & Summers (1969). The
 259 conclusion is that suppression can be large, tends to be greatest for lower ionization stages, but there
 260 is considerable scatter introduced by the details of the atomic structure.

261 3.4. Photoionization models of AGN broad emission-line regions

262 Cloudy includes a large test suite that allows for autonomous testing of the code’s predictions. This
 263 includes a number of models of the “BLR”, the broad emission-line line region of a quasar (AGN3).
 264 Because of their great luminosity, spectra of very high redshift quasars can be used to measure the
 265 chemical evolution of universe and the growth of black holes at the centers of galaxies across cosmic
 266 time. The BLR is photoionized, as shown by correlations between changes in the continuum and
 267 emission lines, and has densities ranging from $10^9 - 10^{14} \text{ cm}^{-3}$, densities where suppression of DR
 268 is expected to be significant, as originally pointed out by Davidson (1975). The Cloudy test suite
 269 includes many BLR models and here we will focus on a subset similar to those discussed in the figures
 270 in (Korista et al. 1997).

271 A photoionization model is parameterized by the shape of the incident ionizing radiation field
 272 or SED, the cloud density and column density, its chemical composition, and either the ionization
 273 parameter or flux of ionizing photons striking the cloud’s surface. We use the SED and composition
 274 given by (Korista et al. 1997) and consider different densities and radiation field intensities. Table 3
 275 shows the impact of suppressed DR on predicted line intensities for a number of different BLR models.
 276 The first column gives the identification of various strong UV emission lines. The remaining columns
 277 are for different BLR model parameters. Each model has a hydrogen density $n(\text{H}) [\text{cm}^{-3}]$ and flux of
 278 ionizing photons $\Phi(\text{H}) [\text{cm}^{-2} \text{ s}^{-1}]$ indicated in the first row as a log. Cloudy includes a user-adjustable
 279 option to set the suppression factors to unity. Otherwise the suppression factor appropriate for the
 280 density and temperature at each point in the cloud is used. The remainder of the table gives the
 281 ratio of the predicted line intensities with, and without, suppression of DR.

Table 3. Ratio of BLR line intensities computed with and without DR suppression.

line\model	9, 18	9, 20	11, 20	12, 19	13, 18	13, 22	14, 18	14, 20	14, 22
O VI 1034	0.98	0.85	0.72	–	–	0.68	–	–	0.50
N V 1240	0.98	1.21	0.78	–	–	0.80	–	0.70	0.56
H I 1216	1.00	0.99	1.03	1.00	1.00	0.98	1.00	1.00	1.03
Si IV 1397	1.02	1.05	1.02	0.80	1.00	0.95	–	0.92	0.83
C IV 1549	0.99	1.04	0.96	0.79	–	0.99	–	0.85	0.88
O III] 1666	0.99	2.33	1.15	0.94	1.01	1.13	1.05	1.02	0.98
Al III] 1860	1.00	1.15	1.04	0.73	0.92	0.97	0.93	0.82	0.83
C III] 1909	1.00	1.66	1.27	0.92	0.95	1.37	0.99	0.90	1.02

283 The ionization parameter U is proportional to the ratio of $\Phi(\text{H})$ to $n(\text{H})$ so, at a given density,
284 increases as $\Phi(\text{H})$ increases. High-ionization species such as C IV, N V, or O VI are not present at low
285 U and the table has no entry for these lines. The table shows that line intensities generally change by
286 less than a factor of two. The changes in the intensities are the result of a complex interplay between
287 temperature, ionization, and density, and simple trends are not obvious. As the flux of ionizing
288 photons increases the temperature of the gas also tends to increase, making DR more important, but
289 the ionization also increases, with DR suppression becoming less important (the q^{-7} effect shown in
290 Figure 2). The net effect depends on all of these details. We stress that the DR suppression factors
291 are highly uncertain so the changes listed in Table 3 are only an indication of the types of changes
292 that might occur if a true CRM were done. This is a high priority for future development.

293 4. SUMMARY

294 We report on revised and improved Paper I DR suppression factors, which are to be used as a
295 preliminary test of the extent the finite densities will likely have on the effective DR rate coeffi-
296 cients. The first group of revisions eliminates potential numerical instabilities which arise in Cloudy
297 simulations and/or modeling that use them. These instabilities are a consequence of assumptions
298 introduced in Paper I for the lowest five isoelectronic sequences and, on finer numerical grids, may

299 manifest themselves as temperature and density discontinuities. The second group of revisions ex-
 300 tends the applicability of suppression factor model to isoelectronic sequences for which secondary
 301 autoionization plays an important role. Improvements are mainly in reproducibility of collisional-
 302 radiative data (Summers 1974 & 1979), in particular the better prediction of activation densities
 303 that mark the onset of suppression of zero-density DR rate coefficients. As such, the present results
 304 are to be used with care outside the Cloudy program, especially if applied to zero-density DR rate
 305 coefficients obtained by neglecting the effect of secondary autoionization where care should be taken
 306 to select the appropriate expression for the suppression factor, as discussed in Sec. 2. Despite the
 307 approximations, we stress the importance of density effects on DR processes in astrophysical plasmas
 308 and need for detailed collisional-radiative calculations.

309 5. ACKNOWLEDGMENTS

310 TWG was supported in part by NASA (NNX11AF32G and NNX17AD41G). KTK was supported in
 311 part by NASA (NNX11AF32G). MC acknowledges support from NASA Program number HST-AR-
 312 14556.001-A through a grant from the Space Telescope Science Institute. GJF acknowledges support
 313 by NSF (1108928; and 1109061), NASA (10-ATP10-0053, 10-ADAP10-0073, and NNX12AH73G),
 314 and STScI (HST-AR-12125.01, GO-12560, and HST-GO-12309). FG acknowledges support by
 315 NSF (1412155). PvH was supported by the Belgian Federal Science Policy Office under contract
 316 No. BR/143/A2/BRASS. NRB acknowledges support by STFC (ST/J000892/1).

REFERENCES

- | | | |
|---|-------------------|--|
| 317 Badnell, N. R., Ferland, G. J., Gorczyca, T. W.,
318 Nikolić, D., & Wagle, G. A. 2015, ApJ, 804, 10,
319 doi: 10.1088/0004-637X/804/2/100 | 323
324
325 | Bates, D. R., Kingston, A. E., & McWhirter,
R. W. P. 1962, Proc. R. Soc. Lond. A, 267, 297,
doi: 10.1098/rspa.1962.0101 |
| 320 Badnell, N. R., O’Mullane, M. G., Summers,
321 H. P., et al. 2003, A&A, 406, 1151,
322 doi: 10.1051/0004-6361:20030816 | 326
327
328 | Blaha, M. 1972, Astrophysical Letters, 10, 179
Burgess, A., & Summers, H. P. 1969, ApJ, 157,
1007, doi: 10.1086/150131 |

- 329 Davidson, K. 1975, ApJ, 195, 285, 349
330 doi: [10.1086/153328](https://doi.org/10.1086/153328) 350
- 331 Ferland, G. J., Chatzikos, M., Guzmán, F., et al. 351
332 2017, Revista Mexicana de Astronomia y 352
333 Astrofisica, 53, 385, 353
334 doi: [http://www.astroscu.unam.mx/rmaa/](http://www.astroscu.unam.mx/rmaa/RMxAA..53-2/PDF/RMxAA..53-2_gferland.pdf) 354
335 [RMxAA..53-2/PDF/RMxAA..53-2_gferland.pdf](http://www.astroscu.unam.mx/rmaa/RMxAA..53-2/PDF/RMxAA..53-2_gferland.pdf) 355
- 336 Hubeny, I., & Mihalas, D. 2014, Theory of Stellar 357
337 Atmospheres An Introduction to Astrophysical 358
338 Non-equilibrium Quantitative Spectroscopic 359
339 Analysis, Princeton Series in Astrophysics (41 360
340 William Street, Princeton, New Jersey 08540: 361
341 Princeton University Press) 362
- 342 Kaur, J., Gorczyca, T. W., & Badnell, N. R. 2017 363
343 A&A, doi: [10.1051/0004-6361/201731243](https://doi.org/10.1051/0004-6361/201731243) 364
- 344 Korista, K., Baldwin, J., Ferland, G., & Verner, 365
345 D. 1997, ApJS, 108, 401, doi: [10.1086/312966](https://doi.org/10.1086/312966) 366
- 346 Nikolić, D., Gorczyca, T. W., Korista, K. T., 368
347 Ferland, G. J., & Badnell, N. R. 2013, ApJ, 768 369
348 1, doi: [10.1088/0004-637X/768/1/82](https://doi.org/10.1088/0004-637X/768/1/82) 370
- Osterbrock, D. E., & Ferland, G. J. 2006,
Astrophysics of Gaseous Nebulae and Active
Galactic Nuclei, 2nd edn. (Sausalito, CA:
University Science Books)
- Ralchenko, Y. 2016, Springer Series on Atomic,
Optical, and Plasma Physics, Vol. 90,
Validation and Verification of
Collisional-Radiative Models, ed. Y. Ralchenko
(Springer International Publishing), 181–208
- Ralchenko, Y., Kramida, A. E., Reader, J., &
NIST ASD Team. 2011, National Institute of
Standards and Technology
- Summers, H. P. 1974 & 1979, Appleton
Laboratory Internal Memorandum IM367 &
re-issued with improvements as AL-R-5
— . 2004, The ADAS User Manual, version 2.6,
doi: <http://www.adas.ac.uk>
- Summers, H. P., & Hooper, M. B. 1983, Plasma
Physics, 25, 1311,
doi: [10.1088/0032-1028/25/12/303](https://doi.org/10.1088/0032-1028/25/12/303)
- Young, P. R. 2018, ApJ, 855, 15,
doi: [10.3847/1538-4357/aaab48](https://doi.org/10.3847/1538-4357/aaab48)

APPENDIX

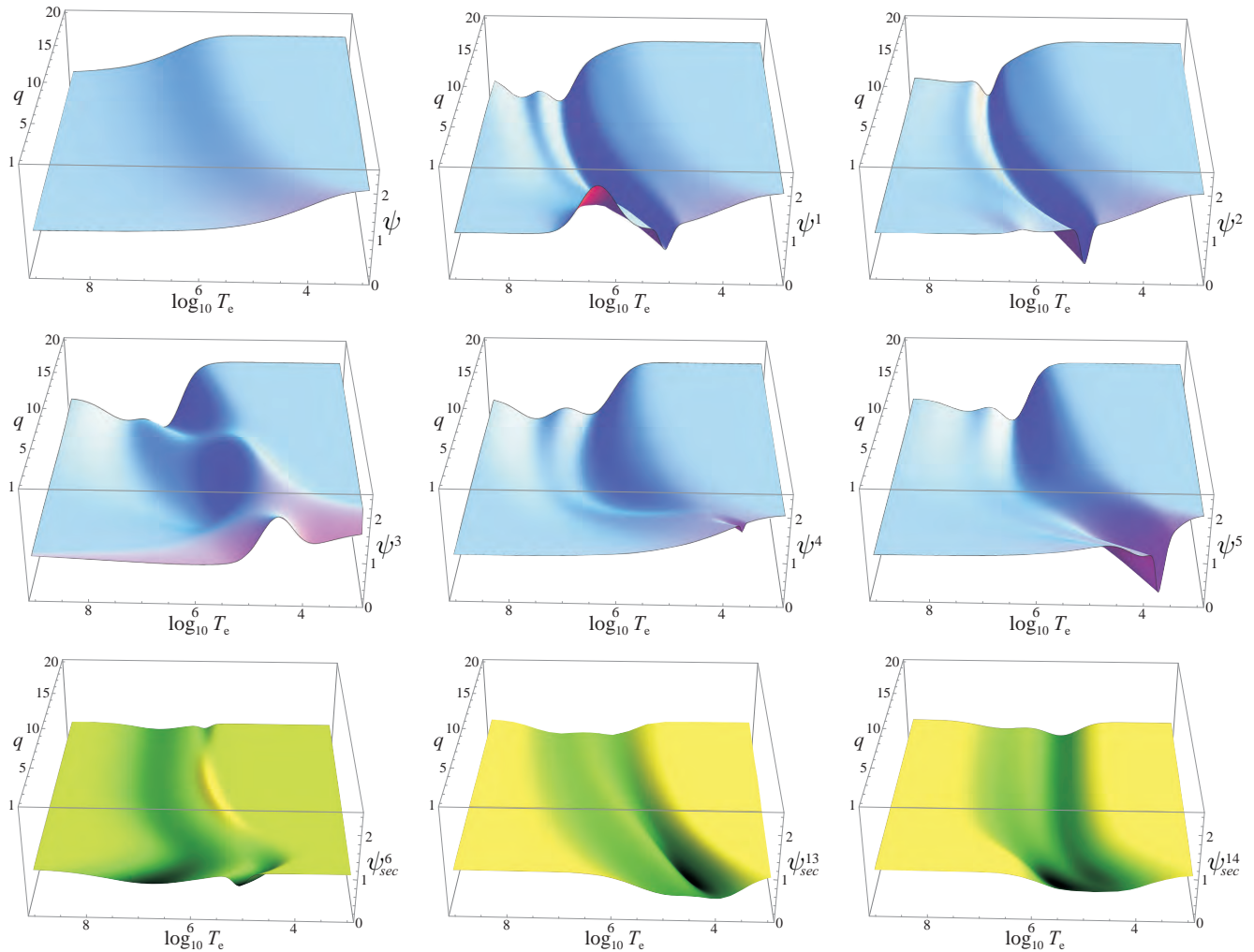
A. VISUALIZATION OF APPROXIMATIONS TO $\psi^N(Q, T)$ 

Figure 4. Illustration of adjustment factors given in Table 2: (top left) “simplified” ψ and (top/middle) “detailed” $\psi^N(q, T)$ factors given in Eq. (10); (bottom) “secondary autoionization” $\psi^N_{sec}(q, T)$ given in Eq. (11).

B. ACCURACY OF APPROXIMATIONS TO $\psi^N(Q, T)$

Figure 5 illustrates the 2- σ (95.4%) confidence levels in reproducing the suppression factors of Summers (1974 & 1979) for several charge states as a function of electron temperature. Higher electron number densities, for which the three-body recombination becomes a dominant process at low θ values, are excluded from 2- σ estimates. Top panels illustrate the accuracies for select ions

Table 4. Values of “detailed” $\psi^N(q, T)$ and “secondary autoionization” $\psi_{sec}^N(q, T)$ given at specified N , q , and T for checking computer code.

$\log_{10} T_e$	$\psi^1(7, T)$	$\psi^2(6, T)$	$\psi^3(5, T)$	$\psi^4(4, T)$	$\psi^5(3, T)$	$\psi_{sec}^5(3, T)$	$\psi_{sec}^6(2, T)$	$\psi_{sec}^{13}(3, T)$	$\psi_{sec}^{14}(2, T)$
4.0	1.99997	1.99985	2.00606	1.9964	1.97356	0.996451	0.99851	0.665474	0.735488
4.5	1.99604	1.9904	2.236	1.94375	1.49331	0.945171	0.845034	0.352422	0.592158
5.0	1.94122	1.90513	2.49967	1.70856	1.01333	0.976266	0.934901	0.594999	0.580803
5.5	1.75124	1.68622	1.5975	1.35216	1.11084	0.999676	0.871361	0.556274	0.509677
6.0	1.39431	1.1391	0.994997	1.14642	1.09561	0.921143	0.774866	0.659487	0.749839
6.5	0.547837	0.91716	0.914818	0.994872	1.10643	0.999988	0.753717	0.822447	0.973149

378 using the methodology of Paper I, with adjustment factor $A^{mod,old}(N)$ given in Eq. (8) and Table 1.
379 Bottom panels are corresponding accuracies from the present study: in the left column are results
380 for “simplified” ψ and in the right column for “detailed” $\psi^N(q, T)$ adjustment factors, both given in
381 Eq. (10) and Table 2. In general, when compared to accuracies of Paper I, the use of “simplified”
382 ψ adjustment factor maintains or slightly improves the accuracy for suppression factors for wide
383 range of temperatures. Most importantly, it removes the discontinuity in suppression factors at low-
384 temperatures as introduced in Paper I for isoelectronic sequences below C-like. When activation log
385 densities $x_a(T; q, N)$ given in Eq. 3 are evaluated using the “detailed” $\psi^N(q, T)$ adjustment factors
386 the overall accuracy improves to better than 14 %.

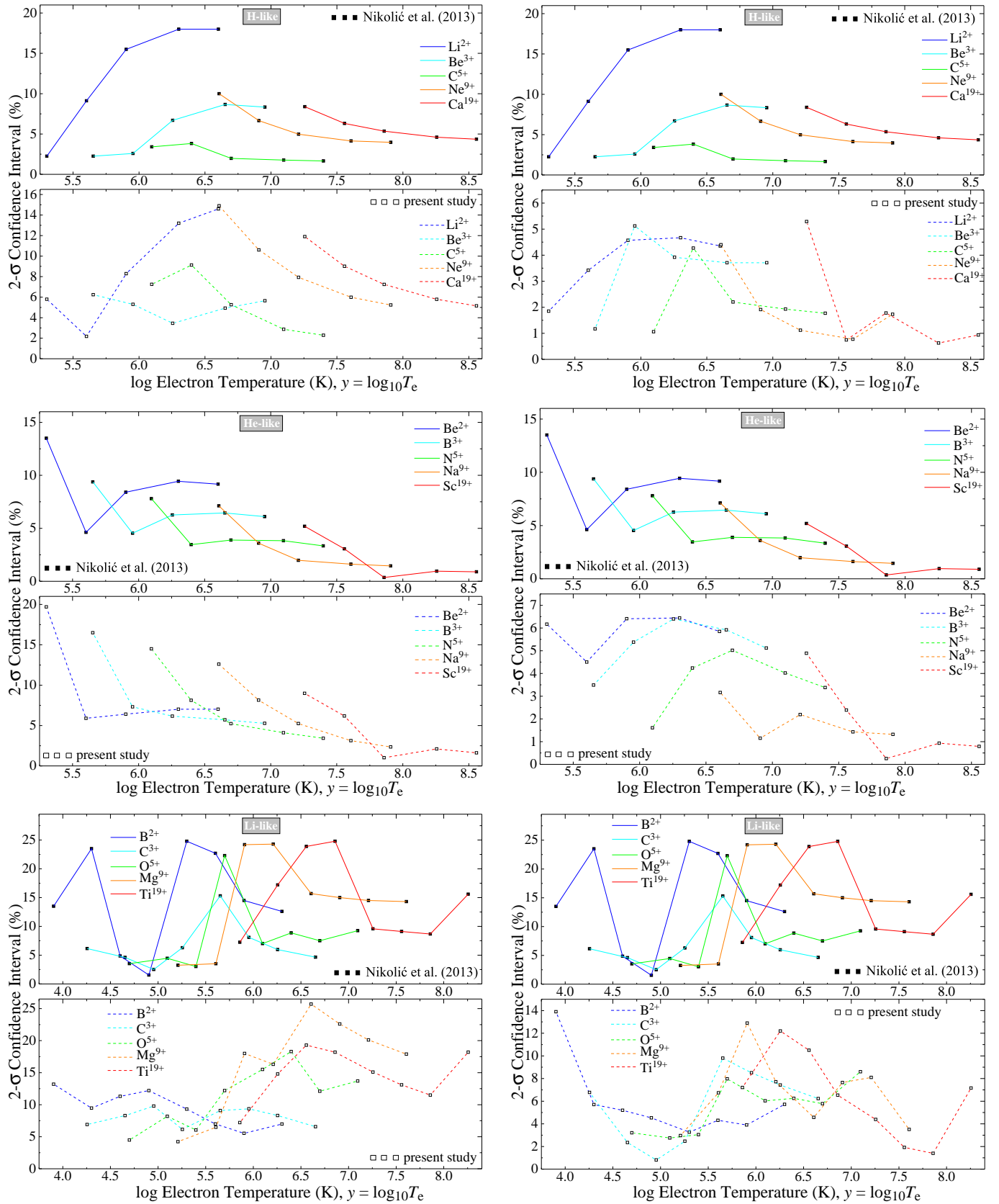


Figure 5. Estimated accuracy for suppression factors for several charge states as a function of electron temperature when different activation log densities are used. See text for details.

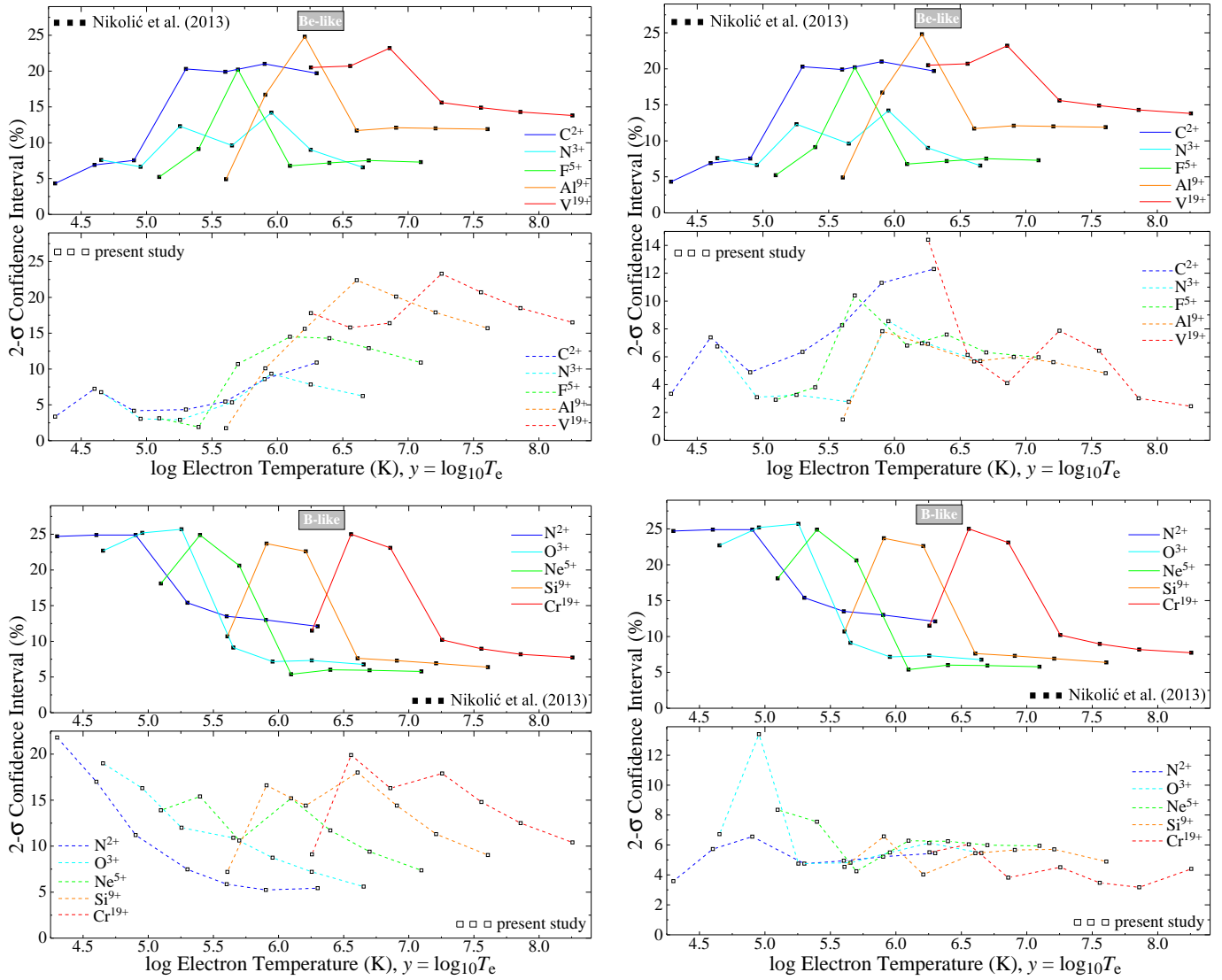


Figure SM-5 (Cont.).

Table 5. Fitting coefficients for the excitation energies $\epsilon_N(q) = \sum_{j=0}^5 p_{N,j} \left(\frac{q}{10}\right)^j$, in eV (see Eq. 16). Numbers in square brackets denote powers of 10.

Sequence	N	$p_{N,0}$	$p_{N,1}$	$p_{N,2}$	$p_{N,3}$	$p_{N,4}$	$p_{N,5}$
Li-like	3	1.963[+0]	2.030[+1]	-9.710[-1]	8.545[-1]	1.355[-1]	2.401[-2]
Be-like	4	5.789[+0]	3.408[+1]	1.517[+0]	-1.212[+0]	7.756[-1]	-4.100[-3]
N-like	7	1.137[+1]	3.622[+1]	7.084[+0]	-5.168[+0]	2.451[+0]	-1.696[-1]
Na-like	11	2.248[+0]	2.228[+1]	-1.123[+0]	9.027[-1]	-3.860[-2]	1.468[-2]
Mg-like	12	2.745[+0]	1.919[+1]	-5.432[-1]	7.868[-1]	-4.249[-2]	1.357[-2]
P-like	15	1.428[+0]	3.908[+0]	7.312[-1]	-1.914[+0]	1.051[+0]	-8.992[-2]
H-, He-, Ne-like	1,2,10	†	0.0	0.0	0.0	0.0	0.0
B-, C-, O-, F-like	5,6,8,9	0.0	0.0	0.0	0.0	0.0	0.0
Al-, Si-, S-, Cl-like	13,14,16,17	0.0‡	0.0	0.0	0.0	0.0	0.0
	≥ 18	0.0	0.0	0.0	0.0	0.0	0.0

† $20 \operatorname{erfc}(2(x - x_a^0))$; ‡ set to 17.6874 for Si-like S^{2+} , see [Badnell et al. \(2015\)](#).

C. EXCITATION ENERGIES $\epsilon_N(Q)$

With respect to Paper I, we update Table 5 with the ion-core excitation energy for Si-like S^{2+} ion to include the study of [Badnell et al. \(2015\)](#).

D. EXAMPLES OF CLOUDY 17 MODEL APPLICATIONS

D.1. *Elemental Abundances using $\psi^N(q, T)$ and $\psi_{sec}^N(q, T)$ adjustment factors*

Figure A illustrates finite-density effect on the collisional ionization fractional abundance on all ionization stages of elements up to and including Zn. All results correspond to “detailed” adjustment factor $\psi^N(q, T)$ given in Eq. (10) and Table 2, and where appropriate, to “secondary autoionization” $\psi_{sec}^N(q, T)$ adjustment factor given in Eq. (11) and Table 2. The solid and dashed curves in upper panels correspond to electron densities of 1 cm^{-3} and 10^{10} cm^{-3} , respectively. From left to right, the curves range from electrically neutral (green) to fully ionized atoms (red). Lower panels in Figure A point to the most effected ionization stages by investigating the ratio of the calculated fractional abundances for the two densities. Similarly, Figure B summarizes finite-density effect at constant-temperature ($\log_{10} T_e = 4.5$) on photoionization fractional abundance as a function of ionization parameter $\log_{10} U$.

Fig. Set A. collisional ionization fractional abundances

Fig. Set B. photoionization fractional abundances

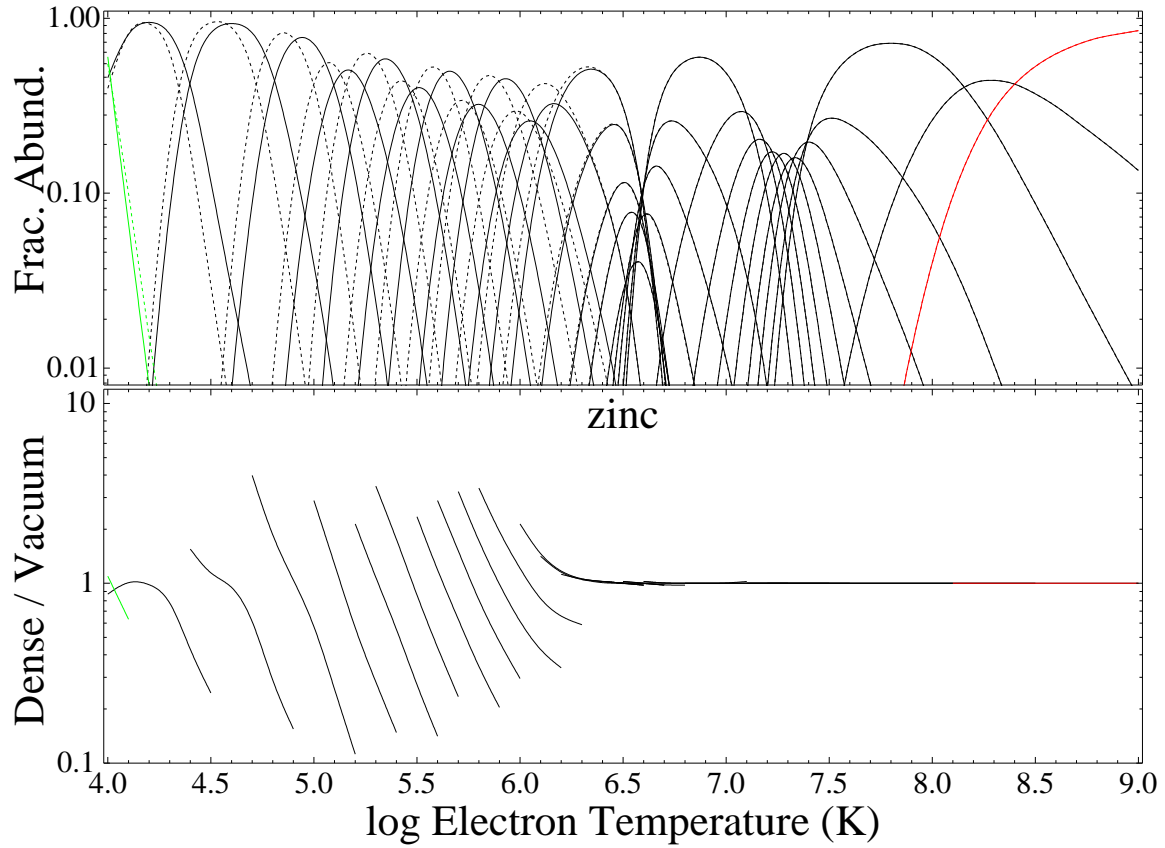


Figure A. Upper panels: collisional ionization fractional abundance vs. electron temperature for all ionization stages of indicated elements. Lower panels: ratio of the calculated fractional abundances for the two densities. The complete figure set (30 images) is available in the online journal.

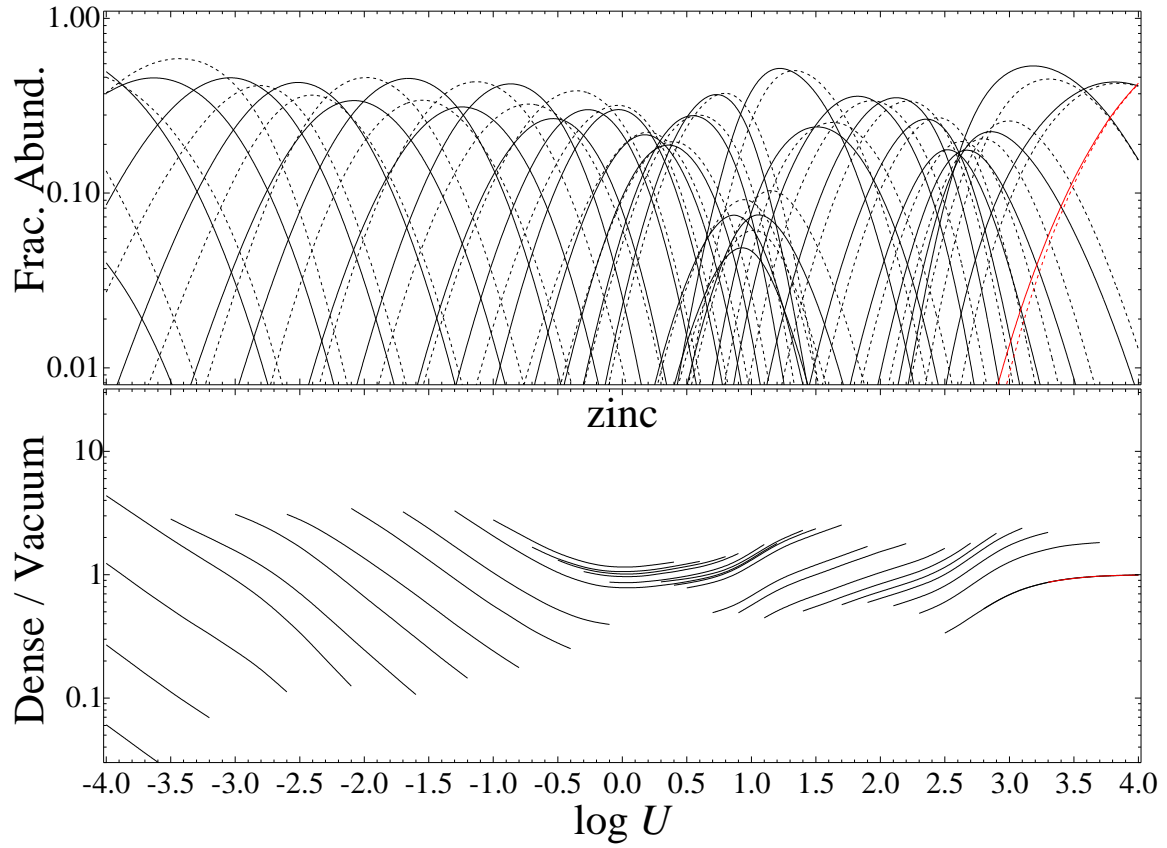


Figure B. Upper panels: photoionization fractional abundance vs. the ionization parameter U for all ionization stages of indicated elements and for constant temperature $\log_{10} T_e = 4.5$. Lower panels: ratio of the calculated fractional abundances for the two densities. The complete figure set (30 images) is available in the online journal.